Acousto–defect interaction in irradiated and non-irradiated silicon n^+–p structures

O. Ya. Olikh,[a] A. M. Gorb, R. G. Chupryna, and O. V. Pristay-Fenenkov
Faculty of Physics, Taras Shevchenko National University of Kyiv, Kyiv 01601, Ukraine

(Received 22 August 2017; accepted 30 November 2017; published online 24 January 2018)

The influence of ultrasound on current–voltage characteristics of non-irradiated silicon n^+–p structures as well as silicon structures exposed to reactor neutrons or ^{60}Co gamma radiation has been investigated experimentally. It has been found that the ultrasound loading of the n^+–p structure leads to the reversible change of shunt resistance, carrier lifetime, and ideality factor. Specifically, considerable acoustically induced alteration of the ideality factor and the space charge region lifetime was observed in the irradiated samples. The experimental results were described by using the models of coupled defect level recombination, Shockley–Read–Hall recombination, and dislocation-induced impedance. The experimentally observed phenomena are associated with the increase in the distance between coupled defects as well as the extension of the carrier capture coefficient of complex point defects and dislocations. It has been shown that divacancies and vacancy–interstitial oxygen pairs are effectively modified by ultrasound in contrast to interstitial carbon–interstitial oxygen complexes. *Published by AIP Publishing.*
https://doi.org/10.1063/1.5001123

I. INTRODUCTION

It is well known that ultrasound (US) can effectively interact with defects. As a defect engineering tool, US has the following advantages: (i) locality of action due to predominant absorption in the regions of lattice periodicity deviation; (ii) selectivity of influence, which depends on acoustic wave (AW) polarization and AW type; (iii) possibility to transform the defect system by applying resonance frequency; and (iv) reversibility of the effect of low intensity AW.

In piezoelectric semiconductors, the acousto–defect interaction (ADI) is mainly determined by the electric field that accompanies the vibration wave propagation. However, the ADI is also observed in such non-piezoelectric crystals as silicon, the basic material in microelectronics. It was experimentally observed that US can cause atomic diffusion,[1,2] transformation of native and impurity defects,[3–7] modification of interior surface states,[8–10] and appearance of new defects[11,12] in Si structures. Defects are known to determine most of the semiconductor device characteristics. In particular, the ADI governs the variation of tunneling,[13,14] generation–recombination,[15–17] and thermionic emission[18,19] currents in silicon barrier structures.

The change of population of impurity oscillator levels,[20] the displacement of impurity atoms with respect to their surroundings,[4,21,22] the decrease in the diffusion activation energy,[23] the local temperature increase caused by point defect clusters,[24] and the US absorption by dislocations[16,25,26] are believed to be the main mechanisms of elastic vibration–defect interactions in non-piezoelectric crystals. However, to the best of our knowledge, there is no comprehensive ADI theory for silicon suggested so far, the lack of experimental research focused on acoustically induced (AI) effects being one of the main reasons.

The defects in silicon structures are not all acoustically active (AA) and can remain unmodified under the action of ultrasound. The ADI efficiency depends on the defect type and structure.[8] For example, the force acting on the point defect in the crystal under US loading (USL) is determined by the relaxation of the defect volume.[21,22] The alterations of semiconductor defects are most widely produced by using the well-studied irradiation method. On the one hand, the high-power US treatment of irradiated silicon structures has been shown[27–30] to result in residual changes in structure properties. This effect deals with AI annealing of radiation defects (RDs). On the other hand, irradiation can be the reason of reversible AI phenomenon initiation,[31,32] which is caused by the formation of acoustically active RDs. Unfortunately, there are but a few reports on the acoustically driven phenomenon in irradiated silicon structures.

The aim of our work is to investigate experimentally the AI electrical characteristic variation that takes place in non-irradiated and irradiated n^+–p-Si structures. For this purpose, the samples were irradiated by reactor neutrons and ^{60}Co–gamma source rays. It is supposed that γ-rays introduce predominantly the VO_i complex,[33–35] whereas neutrons mainly create vacancy clusters,[36,37] disordered regions,[38] and C_iO_i complexes.[35,39] Our work presents distinctions between AI effects in silicon structures with different RDs. The intensity of US applied was insufficient for a new defect formation, RD annealing, or long distance (a many interatomic distance) diffusion. As a result, the complete recovery of characteristics was observed after AW propagation had stopped. To describe the processes in the space charge region (SCR) and in the diode base as well as to study shunt resistance, we used the models of coupled defect level recombination,[40,41] Shockley–Read–Hall (SRH) recombination, and

[a]Electronic mail: olikh@univ.kiev.ua

TABLE I. The sample irradiation parameters.

Sample	Irradiation Type	D (rad)	Ψ (cm^{-2})	NIEL[a] (MeV cm^2/g)	$\Psi \times$ NIEL (MeV/g)
iSC	Non	0	0	…	0
nSC	neutron	4.5×10^3	4×10^{11}	2.04×10^{-3}	8.2×10^8
g6SC	γ–^{60}Co	1×10^6	1.6×10^{15}	1.07×10^{-7}	1.7×10^8
g7SC	γ–^{60}Co	1×10^7	1.6×10^{16}	1.07×10^{-7}	1.7×10^9

[a]Reference 44.

dislocation-induced impedance,[42,43] respectively. The observed AI phenomena are accounted for in terms of the defect interaction with the AW strain field.[21,22] Our research not only provides a better understanding of ADI but could also facilitate the development of acoustically controlled devices or radiation sensors.

II. EXPERIMENTAL AND CALCULATION DETAILS

The n^+–p-Si structure was fabricated from a 2 in. (300 μm thick) p-type boron doped Czochralski silicon wafer with ⟨111⟩ orientation and a resistivity of 10 Ω· cm. The n^+ emitter with a carrier concentration of about 10^{19} cm^{-3} and a thickness of 0.5 μm was formed by phosphorus implantation. The front and rear aluminium electrodes were deposited by screen printing before rapid annealing. The samples used in the experiment were cut from the central part of the wafer and had the area of 2 cm^2. The samples were irradiated by reactor neutrons or by ^{60}Co γ-rays. The doses D, fluences Ψ, and sample labels are listed in Table I. To determine D and Ψ correlation, the data from Refs. 44 and 45 were used. The non-ionizing energy losses (NIEL) for neutron and γ–^{60}Co are also shown in Table I. Since the displacement damage effect is characterized by $(\Psi \cdot \mathrm{NIEL})$, a similar damage was expected in the investigated samples as well. To avoid the impact of long-term annealing, which is typical for the neutron damaged structure,[35,36] the irradiated samples were stored for five years at room temperature before the measurements.

The dark forward current–voltage (I–V) characteristics of the samples both with and without USL were measured over a temperature range of 290–340 K. The temperature was controlled by a differential copper–constantan thermocouple. Some of the obtained curves are shown in Fig. 1.

The double-diode model of n^+–p structure I–V characteristics is expressed in the following form:

$$I(V,T) = I_{SCR} + I_{base} + I_{sh}, \tag{1}$$

$$I_{SCR} = \frac{qAn_i d}{2\tau_g}\left\{\exp\left[\frac{q(V-IR_s)}{n_{\mathrm{id}}kT}\right]-1\right\}, \tag{2}$$

$$I_{base} = \frac{qAn_i^2}{p_p}\sqrt{\frac{\mu_n kT}{\tau_n}}\left\{\exp\left[\frac{q(V-IR_s)}{kT}\right]-1\right\}, \tag{3}$$

$$I_{sh} = (V-IR_s)/R_{sh}, \tag{4}$$

where I_{SCR} describes the overall SCR recombination, I_{base} is closely related to the recombination in the quasi-neutral region, I_{sh} is the shunt current, A is the sample area, n_i is the intrinsic carrier concentration, τ_g is the SCR carrier lifetime, d is the SCR thickness

$$d = \sqrt{\frac{2\varepsilon\varepsilon_0}{qp_p}\left[\frac{E_g}{q}-\frac{kT}{q}\ln\left(\frac{N_vN_c}{p_pn_n}\right)-\frac{2kT}{q}-V\right]}, \tag{5}$$

ε is the permittivity (11.7 for Si), p_p and n_n are the majority carrier concentration in p- and n-type regions, E_g is the semiconductor bandgap, N_c and N_v are the effective densities of states in the conduction and valence bands; n_{id} is the ideality factor, R_s and R_{sh} are the series and shunt resistances, and μ_n and τ_n are the mobility and lifetime of the electron (minority carrier) in the diode base.

We used Eqs. (1)–(5) to fit the experimental data taking τ_g, τ_n, n_{id}, R_{sh}, and R_s as the fitting parameters. Also, we used the known[46–48] temperature dependences of n_i, E_g, and μ_n. As a result, we obtained extremely good fit to the experimental data—see Fig. 1. In particular, for all the samples, the value of R_s was found to be about 1 Ω. The broken lines in Fig. 1(a) show an example of the calculated contributions of I_{SCR}, I_{base}, and I_{sh} to the total current.

In the case of USL, the transverse AWs with the frequency of 4.2 MHz, which were excited by using a piezoelectric transducer, were applied to the samples at the base side in the [111] direction. The US intensities W_{US}, amplitudes of lattice deformation ξ_{US}, and lattice atom displacements u_{US} are listed in Table II. It was reported previously[6,7,19] that the characteristic time of change in

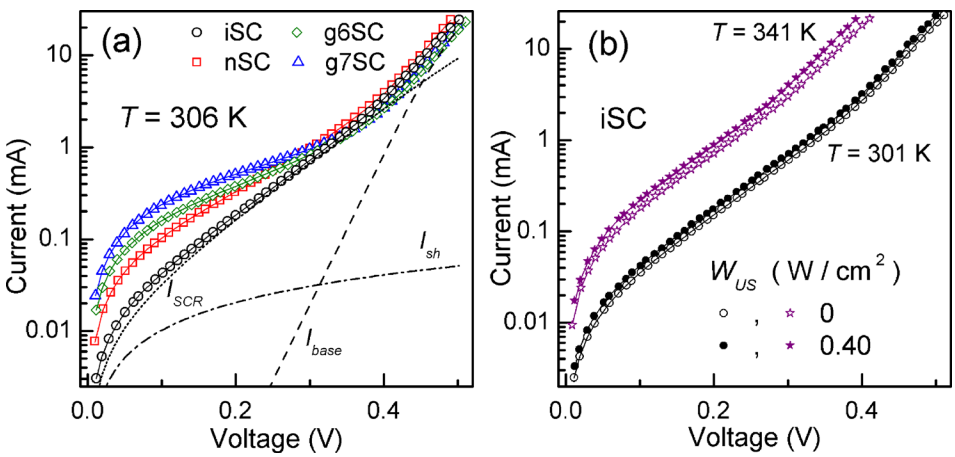

FIG. 1. Dark I–V characteristics measured (a) at 306 K for non-irradiated (circles), neutron-irradiated (squares), and gamma-irradiated (diamonds and triangles) structures without USL; (b) at 301 K (circles) and 341 K (asterisks) with (filled marks, Ui-2) and without (open marks) USL for the iSC. The marks are the experimental results, and the solid lines are the curves fitted by Eqs. (1)–(5). The dashed, dotted, and dotted–dashed lines in (a) represent the calculated base, SCR, and shunt components of total iSC current (black solid line).

TABLE II. The ultrasound loading parameters.

Sample	W_{US} (W/cm^2)	ξ_{US} (10^{-6})	u_{US} (nm)	USL label
iSC	0.22	3.1	0.67	Ui-1
	0.40	4.2	0.91	Ui-2
nSC	0.24	3.2	0.70	Un-1
	0.40	4.2	0.91	Un-2
g6SC	0.38	4.1	0.89	Ug6-2
g7SC	0.19	2.9	0.63	Ug7-1
	0.37	4.0	0.87	Ug7-2

silicon structure parameters under the US action did not exceed 2×10^3 s. In order to wait until the AI transitional period is completed, the following experimental procedure was used. When USL started, the sample was first exposed to room temperature for 60 min and then the *I–V* measurement and the sample heating were started. In order to avoid the effect of the piezoelectric field on *I–V* characteristics, the piezoelectric transducer was shielded.

Figure 2 illustrates the reversibility of AI effects. The time interval between USL initiation and "during" measurement was longer than 60 min, and the time interval between USL termination and "after" measurement was about 24 h. The data for nSC and g6SC are similar to those presented for iSC and g7SC.

The non-linear fittings were performed by using the differential evolution method.[49]

III. RESULTS AND DISCUSSION

A. Space charge region

The parameters of *I–V* characteristics associated with SCR phenomena are n_{id} and τ_g. The temperature dependences of the ideality factor and SCR carrier lifetime are shown in Figs. 3 and 4, respectively.

As shown in Fig. 3, the ideality factor decreases with the increase in temperature, and the dependence of n_{id} on $1/T$ is close to linear. Thus, dependence $n_{id}(T)$ can be expressed as

$$n_{id}(T) = n_{id,\infty} + T_{id}/T\,. \tag{6}$$

The thermoactivated growth of SCR lifetime is observed over the explored temperature range—see Fig. 4. The temperature dependence of τ_g is well described by the following equation:

$$\tau_g(T) = \tau_{g0} \exp\left(-\frac{E_{\tau g}}{kT}\right). \tag{7}$$

The values of T_{id} and $E_{\tau g}$ found for both non-irradiated and irradiated samples under USL as well as without USL are listed in Table III.

We would like to stress that

(i) irradiation leads to changes in T_{id} and $E_{\tau g}$, and g6SC's characteristic temperature of the ideality factor and SCR lifetime characteristic energy are closely related to those of g7SC under similar conditions;

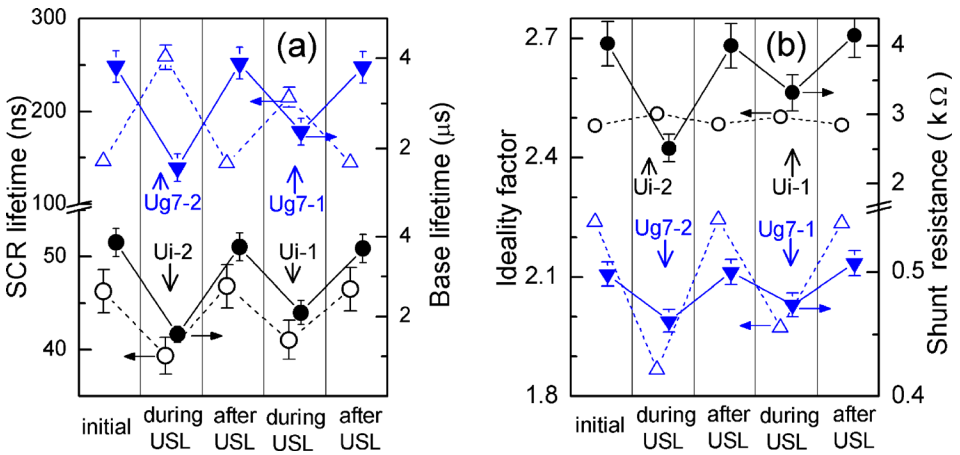

FIG. 2. SCR lifetime (a, left axis, open marks), base lifetime (a, right axis, filled marks), ideality factor (b, left axis, open marks), and shunt resistance (b, right axis, filled marks) obtained before, during, and after USL at 330 K. Data for iSC (circles) and g7SC (triangles) are presented.

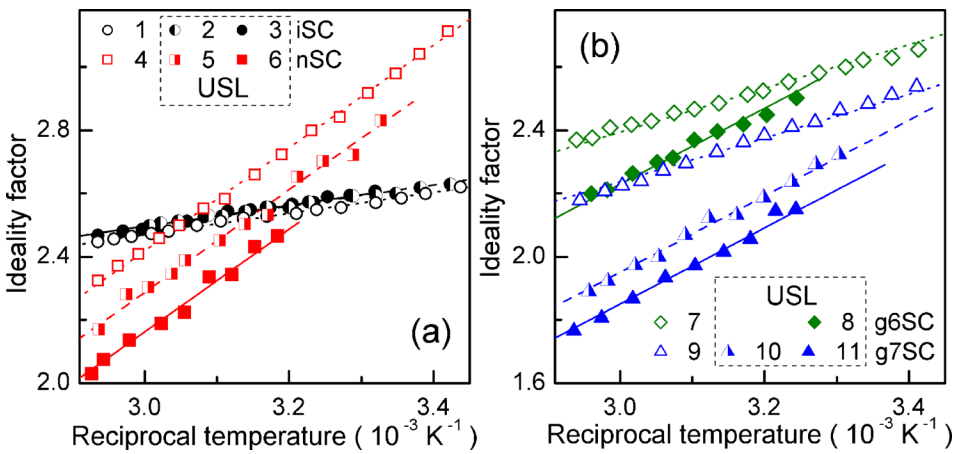

FIG. 3. Temperature dependences of the ideality factor for non-irradiated (curves 1–3, circles), neutron-irradiated (4–6, squares), and γ-irradiated (7–11, diamonds and triangles) samples. The curves 1, 4, 7, and 9 (open marks) are obtained without USL, and curves 2, 3, 5, 6, 8, 10, and 11 correspond to Ui-1, Ui-2, Un-1, Un-2, Ug6-2, Ug7-1, and Ug7-2, respectively. The marks are the experimental results, and the lines are the fitted curves using Eq. (6).

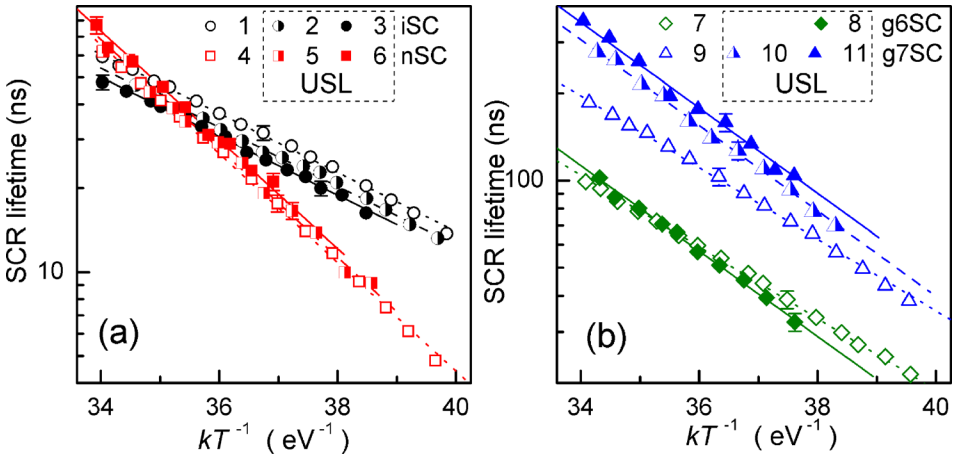

FIG. 4. Temperature dependences of SCR lifetime for non-irradiated (curves 1–3, circles), neutron-irradiated (4–6, squares), and γ-irradiated (7–11, diamonds and triangles) samples. The curves 1, 4, 7, and 9 (open marks) are obtained without USL, and curves 2, 3, 5, 6, 8, 10, and 11 correspond to Ui-1, Ui-2, Un-1, Un-2, Ug6-2, Ug7-1, and Ug7-2, respectively. The marks are the experimental results, and the lines are the fitted curves using Eq. (7).

(ii) USL affects n_{id} and τ_g values; the absolute AI changes of the ideality factor $\Delta n_{\mathrm{id}} = n_{\mathrm{id,US}} - n_{\mathrm{id},in}$ and the relative AI changes of SCR lifetime $\varepsilon_{\tau g} = (\tau_{g,\mathrm{US}} - \tau_{g,in})/\tau_{g,in}$ (where subscripts "US" and "*in*" indicate the values obtained at the same temperature with and without USL, respectively) are listed in Table IV;

(iii) Δn_{id} and $\varepsilon_{\tau g}$ vary with W_{US} enhancement, whereas T_{id} and $E_{\tau g}$ values practically do not depend on US intensity;

(iv) USL leads to the increase in both T_{id} and $E_{\tau g}$ in γ-irradiated samples [see Figs. 3(b) and 4(b)], but this effect is not observed in non-irradiated and neutron-irradiated samples [see Figs. 3(a) and 4(a)];

(v) Δn_{id} and $\varepsilon_{\tau g}$ have opposite signs for non-irradiated and irradiated samples (for SCg6 not in the whole temperature range);

(vi) ideality factor is varied by USL more effectively in the irradiated samples.

For the purpose of our analysis, it is important to discuss the recombination mechanism in SCR of the investigated samples. According to classical SRH theory, the ideality factor must be smaller than 2, and τ_g temperature dependence is expected[50,51] to be described by the relation $\tau_g \simeq 2\,\tau_n \sqrt{\sigma_n/\sigma_p}\cosh[(E_t - E_i)/kT]$ (where σ_n, σ_p, and E_t are the electron and hole capture cross sections (CCSs) and the energy level of the recombination center, and E_i is the intrinsic energy level). In our case, n_{id} is greater than 2, and τ_g increases with temperature. Therefore, SRH theory cannot be applied in our case. Several attempts to account for large n_{id} values have been made by using different models.[52–55] However, all the observed features of SCR recombination (large ideality factor, independence of light intensity, dependence on temperature as well as short carrier lifetime) can be explained by the model of coupled defect level recombination (CDLR)[40,41] only. This mechanism provides a rapid direct charge transfer between defect levels. The phenomenon was first observed experimentally,[56,57] after which it was recruited to explain the process in semiconductor diodes.[40,41,58]

According to the CDLR model, the recombination is the result of carrier exchange between two defect levels and crystal bands. In particular, it is supposed[41] that the recombination rate is dominant at the sites where the acceptor-like defect is coupled with the donor-like defect. In a simplified case, when there is no carrier exchange between the donor level E_t^{D} and the valence band, as well as between the acceptor level E_t^{A} and the conduction band, the recombination rate R can be expressed[40] as

$$R = \frac{R_{12} - \sqrt{R_{12}^2 - 4\tau_n^{\mathrm{D}}\tau_p^{\mathrm{A}}(np - n_i^2)(1-\epsilon)}}{2\tau_n^{\mathrm{D}}\tau_p^{\mathrm{A}}(1-\epsilon)}, \tag{8}$$

$$R_{12} = \frac{(n+n_{\mathrm{D}})(p+p_{\mathrm{A}})}{R_{\mathrm{DA}}} + \tau_n^{\mathrm{D}}(p+p_{\mathrm{D}}) + \tau_p^{\mathrm{A}}(n+n_{\mathrm{A}}), \tag{9}$$

$$\tau_n^{\mathrm{D}} = (N_{\mathrm{D}}\,\sigma_n^{\mathrm{D}}\,v_{\mathrm{th},n})^{-1}, \quad \tau_p^{\mathrm{A}} = (N_{\mathrm{A}}\,\sigma_p^{\mathrm{A}}\,v_{\mathrm{th},p})^{-1}, \tag{10}$$

TABLE III. Characteristics of temperature dependences of n^+–p-Si structure parameters.

Sample	USL	T_{id} (K)	$E_{\tau g}$ (eV)	$R_{293,\mathrm{Al}}$ (kΩ)	σ_{dis} (10^4 K/Ω)
iSC	non	330 ± 30	0.24 ± 0.01	27 ± 3	41 ± 4
	Ui-1	310 ± 30	0.24 ± 0.01	27 ± 3	50 ± 4
	Ui-2	360 ± 30	0.24 ± 0.01	26 ± 3	58 ± 4
nSC	non	1610 ± 70	0.45 ± 0.02	2.2 ± 0.4	65 ± 7
	Un-1	1600 ± 70	0.44 ± 0.02	2.3 ± 0.4	95 ± 10
	Un-2	1680 ± 70	0.44 ± 0.02	2.2 ± 0.4	130 ± 10
g6SC	non	610 ± 40	0.28 ± 0.01	0.7 ± 0.1	19 ± 2
	Ug6-2	1080 ± 50	0.33 ± 0.02	0.8 ± 0.1	24 ± 2
g7SC	non	770 ± 50	0.29 ± 0.01	0.41 ± 0.06	26 ± 3
	Ug7-1	1260 ± 60	0.34 ± 0.02	0.39 ± 0.06	45 ± 4
	Ug7-2	1270 ± 60	0.35 ± 0.02	0.38 ± 0.06	55 ± 4

TABLE IV. Acoustically induced change of n^+–p-Si structure parameters (at 330 K).

Sample	USL	Δn_{id} (±0.01)	$\varepsilon_{\tau g}$ (±5%)	$\varepsilon_{\tau n}$ (±0.2)	$\varepsilon_{\sigma\mathrm{dis}}$ (±10%)
iSC	Ui-1	0.02	−14	0.7	20
	Ui-2	0.03	−17	1.4	40
nSC	Un-1	−0.13	5	1.5	50
	Un-2	−0.26	13	3.0	100
g6SC	Ug6-2	−0.15	2	2.3	30
g7SC	Ug7-1	−0.26	49	0.9	70
	Ug7-2	−0.36	70	1.9	110

where R_{DA} is the coupling parameter, N_D and N_A are the densities of donor and acceptor-like defects, σ_n^D and σ_p^A are the electron CCS of the donor and hole CCS of the acceptor, $v_{th,n}$ and $v_{th,p}$ are the thermal electron and hole velocities, $n_{D,A}$, $p_{D,A}$, and ϵ depend on E_t^D, E_t^A, and level degeneracy factors. Since $\tau_g \propto R^{-1}$, the last three values are expected to provide a thermoactivated behavior of SCR lifetime. Unfortunately, the equation does not account for the functional relation between I–V characteristics parameters and attributes of defects taking part in CDLR.

According to Steingrube *et al.*,[41] CCS for the defect in a pair differs from that for an isolated defect and depends on the distance r between the donor and the acceptor

$$\sigma_{n,p}^{D,A}(r) = C_{n,p}^{D,A}\, r^2, \tag{11}$$

where C_n^D and C_p^A are the constant values. R_{DA} is proportional to the overlap integral of the defect wave functions as well. If both defects are characterized by the H-like radial–symmetric wave function and equal Bohr radius a_0, the following expression can be used:[41]

$$R_{DA}(r) \propto N_D N_A \left[1 + \frac{r}{a_0} + \frac{1}{3}\left(\frac{r}{a_0}\right)^2\right] e^{-r/a_0}. \tag{12}$$

In our opinion, the observed reversible AI modifications of n_{id} and τ_g are induced by donor–acceptor distance alteration in the samples under USL. In fact, according to the data,[21,22] the force acting on a point defect during USL can be expressed as

$$F_d = \chi\, \Delta\Omega_d \frac{\partial \xi(z,t)}{\partial z}, \tag{13}$$

where χ is the bulk elasticity modulus, $\Delta\Omega_d$ is the crystal volume change per defect, ξ is the crystal lattice deformation, and AW propagates along the z axis, $\partial\xi(z,t)/\partial z \propto \xi_{US}$. For the interstitial atoms and substitutional impurities with ionic radius exceeding the ionic radius of matrix atoms, $\Delta\Omega_d > 0$, whereas for the vacancies and substitutional impurities whose ionic radius is smaller than that of matrix atoms, $\Delta\Omega_d < 0$. Therefore, a point defect vibrates under USL, so oscillation amplitude and phase are determined by both the defect character and AW intensity.

The simplest model, which is shown in Fig. 5, gives the following qualitative conclusion. Initially, the donor and the acceptor are separated by the distance r_{in}, and the X axis is drawn through the point defect initial positions. Under USL, the defects would vibrate with amplitudes u_D and u_A. The vibration axis coincides with the AW displacement direction and forms angle φ with the X-axis. Depending on ξ_{US}, defect elastic strain ($\Delta\Omega_d^D$ and $\Delta\Omega_d^A$), and defect coupling, the defect vibration amplitudes can have different values. The donor–acceptor distance in the sample under USL r_{US}, according to the model, depends on time t

$$r_{US}(t) = \Big\{[r_{in} + u_A\cos(\omega_{US}t + \delta) - u_D\cos(\omega_{US}t)]^2\cos^2\varphi + [u_A\cos(\omega_{US}t + \delta) - u_D\cos(\omega_{US}t)]^2\sin^2\varphi\Big\}^{0.5}, \tag{14}$$

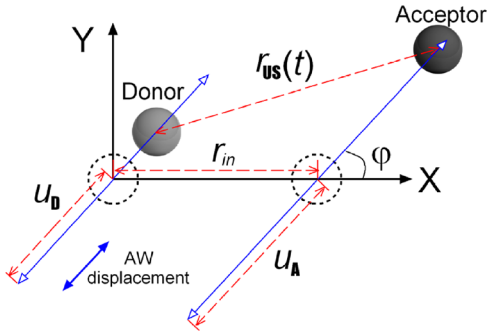

FIG. 5. Model of CDLR center behavior under US action.

where ω_{US} is the US cyclic frequency and δ is the phase shift between donor and acceptor vibration.

We use Eqs. (11) and (12) to estimate AI relative changes of CCS $\varepsilon_\sigma = [\sigma_{US} - \sigma(r_{in})]/\sigma(r_{in})$ and coupling parameters $\varepsilon_{RDA} = [R_{DA,US} - R_{DA}(r_{in})]/R_{DA}(r_{in})$, where σ_{US} and $R_{DA,US}$ are averaged over the AW period T_{US}

$$\sigma_{US} = \frac{1}{T_{US}}\int_0^{T_{US}} \sigma(r_{US}(t))dt,$$
$$R_{DA,US} = \frac{1}{T_{US}}\int_0^{T_{US}} R_{DA}(r_{US}(t))dt.$$

In this estimation, the relaxation time in the CDLR subsystem is assumed to be considerably shorter than T_{US}, and we apply the previously used[41] value $a_0 = 3.23$ nm. In addition, the chosen u_D and u_A values are commensurate with u_{US}. However, it should be taken into account that the displacement of the point defect without the covalent bond could exceed a matrix atom displacement. Finally, no US absorption by the defect is assumed. In this simple case, δ is equal to 0° if $(\Delta\Omega_d^D \cdot \Delta\Omega_d^A) > 0$ or to 180° if $(\Delta\Omega_d^D \cdot \Delta\Omega_d^A) < 0$. In addition, ε_{RDA} exclusively depends on $|u_D - u_A|$ (in the $\delta = 0°$ case) or $|u_D + u_A|$ (in the $\delta = 180°$ case). Moreover, these dependences are identical in both cases. The typical results of simulation of coupling parameter changes are shown in Fig. 6.

Relative changes of CCS depend on oscillation amplitudes with similar features and do not depend on φ

$$\varepsilon_\sigma = (u_D \pm u_A)^2/2r_{in}^2 = K_{US}^{DA} W_{US}, \tag{15}$$

where "+" and "−" correspond to $\delta = 180°$ and $\delta = 0°$, respectively, K_{US}^{DA} characterizes the defect couple–ultrasound interaction and depends on property defects as well as the crystal matrix. Equation (15) takes into account that $u_D, u_A \propto \xi_{US} \propto \sqrt{W_{US}}$.

It is worth keeping in mind that CDLR current flows locally in the locations of extended defects.[41,58] At the same time, the dislocations are often located perpendicularly to the p–n junction plane in the SCR region, and the investigated samples are not exception (see Sec. III C). If coupled defects and dislocations are close to each other, then the dislocations with the edge component should affect the pair spatial orientation. Thus, the axis of donor–acceptor pair with $(\Delta\Omega_d^D \cdot \Delta\Omega_d^A > 0)$ should be predominantly parallel to the dislocation line, whereas the axis of a pair of coupled defects with $(\Delta\Omega_d^D \cdot \Delta\Omega_d^A < 0)$ should make a right angle with the

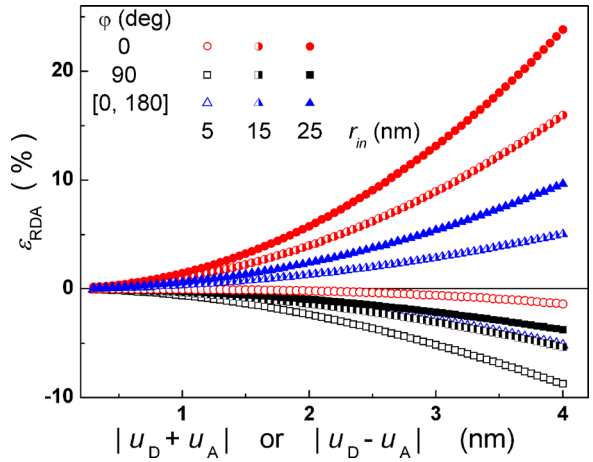

FIG. 6. Simulated dependencies of AI changes of the coupling parameter on the vibration amplitudes. Axis $|u_D - u_A|$ corresponds to the $\delta = 0°$ case, whereas axis $|u_D + u_A|$ corresponds to the $\delta = 180°$ case. The parameters are set to $a_0 = 3.23$ nm, $r_{in} = 5$ nm (open marks), 15 nm (semi-filled marks), and 25 nm (filled marks), and $\varphi = 0°$ (circles) 90° (squares). The triangles correspond to the mean ε_{RDA} value for the $[0° \div 180°]\varphi$ range.

dislocation line. As AW displacement is parallel to the *p–n* junction plane, the cases of most exciting interest are the following:

$$\delta = 0°, \quad \varphi = 90° \left(\Delta\Omega_d^D \cdot \Delta\Omega_d^A > 0 \text{ case}\right);$$
$$\delta = 180°, \quad \varphi \in [0°\text{–}180°] \left(\Delta\Omega_d^D \cdot \Delta\Omega_d^A < 0 \text{ case}\right).$$

In other words, all curves in Fig. 6 can be realized if defect volume relaxation of the donor-like defect has the sign opposite to that of acceptor-like defect. Moreover, only squares should to be under consideration in the case of $\Delta\Omega_d^D \cdot \Delta\Omega_d^A > 0$.

Taking into account the experimental results and the estimation obtained from our model:

(i) $E_{\tau g}$ and T_{id} are mainly determined by couple component energy levels. The alteration of $E_{\tau g}$ and T_{id} for nSC, g6SC, and g7SC in comparison with iSC testifies to the change of defect (donor, acceptor, or both) which take part in CDLR after irradiation. g6SC defects are coincident to g7SC defects and differ from the neutron-irradiated sample defect.

(ii) USL causes the donor–acceptor distance change and results in ε_σ and ε_{RDA}, which increase with W_{US}.

(iii) Acoustically induced $E_{\tau g}$ (and T_{id}) modification, which is observed in g6SC and g7SC only, testifies to the rebuilding of γ-induced RD, i.e., γ-induced RD is configurationally bistable (or metastable) and transforms from the ground state under US action. Similar AI defect variations were also reported previously.[3,5,32,59]

(iv) ε_σ sign is immutable—see Eq. (15), whereas the ε_{RDA} sign can vary for the pair with the opposite relaxation volume component (see Fig. 6). Therefore, the change of Δn_{id} and $\varepsilon_{\tau g}$ sign is the evidence of transformation from $(\Delta\Omega_d^D \cdot \Delta\Omega_d^A > 0)$ to $(\Delta\Omega_d^D \cdot \Delta\Omega_d^A < 0)$ after irradiation. The transformation is confirmed by the enhanced efficiency of US action on defects in irradiated samples. In fact, in the case of $(\Delta\Omega_d^D \cdot \Delta\Omega_d^A < 0)$, the US efficiency is determined by the sum of pair component displacements, whereas in the contrary case, it is determined by their difference. In our opinion, both the donor and the acceptor are defects of interstitial-type in the non-irradiated sample, and one of the pair components is a defect of vacancy-type in irradiated samples. The defect configurations are discussed below, in Sec. III D.

B. Quasi-neutral region

Base lifetime describes the processes which occur in the quasi-neutral region of the *p–n* structure. Figure 7 shows τ_n behaviour in the explored temperature range. As expected, minority carrier lifetime increases as the temperature increases, and at 320 K, τ_n values comprise 2–5 μs for different samples, which correspond to the 80–130 μm range of diffusion lengths. In our opinion, the observed τ_n dispersion is caused not by irradiation but rather deals with sample–ancestor wafer inhomogeneity, which is often the case.[60,61]

In fact, the irradiation induced lifetime reduction is described by the Messenger-Spratt equation[48]

$$\tau_n^{-1} = \tau_{n0}^{-1} + K_\tau \Psi, \tag{16}$$

where τ_{n0} is the minority carrier lifetime in the non-irradiated sample and K_τ is a lifetime damage constant. The known K_τ values and estimated changes of reciprocal base lifetime $K_\tau\Psi$ are shown in Table V. As seen from the table, the estimated value of the radiation-induced τ_n^{-1} change comprises (8–17), 4, and 29% of the values measured for samples nSC, g6SC, and g7SC, respectively, so this cannot explain the dispersion observed experimentally. At the same time, the calculated lifetime changes $K_\tau\Psi$ are in quite good agreement with the changes expected from RDs production—see Sec. III D.

Base lifetime can be expressed as follows:[64]

$$\tau_n^{-1} = \tau_{bb}^{-1} + \tau_{CEAuger}^{-1} + \tau_{SRH}^{-1}, \tag{17}$$

where τ_{bb}, $\tau_{CEAuger}$, τ_{SRH} are the lifetimes of band-to-band recombination, Coloumb-enhanced Auger recombination, and SRH recombination, respectively. The calculation shows that $\tau_{bb}^{-1} = 14\ s^{-1}$ and $\tau_{CEAuger}^{-1} = 6\ s^{-1}$. Therefore, band-to-band recombination and Auger recombination can be neglected. In the case of the low injection level and single recombination centre, SRH lifetime is described by Eq. (10). If there are several centers of recombination, the following equation should be applied:

$$\tau_n^{-1} = \sum_i^{M_d} \tau_{n,i}^{-1} = \sum_i^{M_d} N_{d,i}\sigma_{n,i}\, v_{th,n}, \tag{18}$$

where M_d is the total number of centers, $\tau_{n,i}$ characterizes lifetime due to recombination by the *i*-th defect, and $N_{d,i}$ and $\sigma_{n,i}$ are the concentration and electron CCS of the *i*-th defect, respectively.

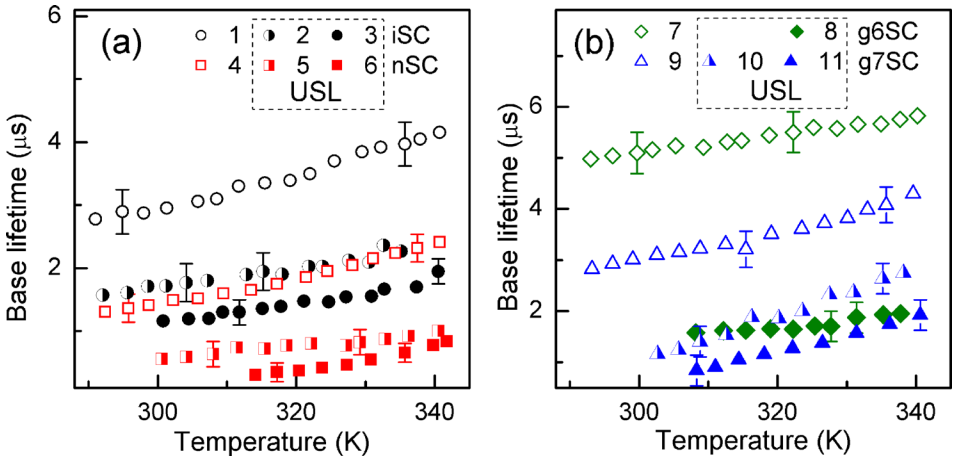

FIG. 7. Temperature dependences of base lifetime for non-irradiated (curves 1–3, circles), neutron-irradiated (4–6, squares), and γ-irradiated (7–11, diamonds and triangles) samples. The curves 1, 4, 7, and 9 (open marks) are obtained without USL, and curves 2, 3, 5, 6, 8, 10, and 11 correspond to Ui-1, Ui-2, Un-1, Un-2, Ug6-2, Ug7-1, and Ug7-2, respectively.

Figure 7 shows that USL results in a decrease in τ_n. Relative AI changes of base lifetime $\varepsilon_{\tau n} = (\tau_{n,in} - \tau_{n,\mathrm{US}})/\tau_{n,\mathrm{US}}$ are listed in Table IV. As AI changes are reversible, the lifetime alteration, in our opinion, deals with the increase in σ_n under US action. Following the empirical relation proposed by Ref. 65, we assume that Eq. (11) is valid for a complex point defect as well. In this case, however, r is the distance which separates the components of a complex. According to the model suggested in Sec. III A, USL leads to r variation and σ_n change in line with Eq. (15). In the case of CDLR, the AI change of the capture cross section of donor (or/and acceptor) is supplemental to the variation of both the coupling parameter and the couple distance, but only the CCS change determines the AI variation of base lifetime.

However, not every defect effectively takes part in AID. If M_d^{AA} and M_d^{nonAA} are the total numbers of acoustically active (AA) and non-acoustically active (non-AA) centers, Eq. (18) for τ_n^{-1} under USL and without it takes the following shape:

$$\tau_{n,in}^{-1} = \sum_j^{M_d^{\mathrm{AA}}} N_{d,j}\sigma_{n,j}^{in}\, v_{\mathrm{th},n} + \sum_l^{M_d^{\mathrm{nonAA}}} N_{d,l}\sigma_{n,l}\, v_{\mathrm{th},n},$$

$$\tau_{n,\mathrm{US}}^{-1} = \sum_j^{M_d^{\mathrm{AA}}} N_{d,j}\sigma_{n,j}^{\mathrm{US}}\, v_{\mathrm{th},n} + \sum_l^{M_d^{\mathrm{nonAA}}} N_{d,l}\sigma_{n,l}\, v_{\mathrm{th},n}.$$

By using Eq. (15), $\varepsilon_{\tau n}$ is transformed as follows:

$$\varepsilon_{\tau n} = K_{\mathrm{US}}^{\mathrm{eff}} W_{\mathrm{US}}, \tag{19}$$

where $K_{\mathrm{US}}^{\mathrm{eff}}$ characterizes ADI in the sample and depends on the concentration of both AA and non-AA centers

TABLE V. Measured and estimated base lifetime parameters.

Sample	$\tau_{n,in}^{-1}$ (320 K)	K_τ	$K_\tau \times \Psi$	$K_{\mathrm{US}}^{\mathrm{eff}}$
	(10^5 s^{-1})	(cm^2/s)	(10^4 s^{-1})	(cm^2/W)
iSC	2.9	…	…	3.5
nSC	4.7	10^{-7}(Ref. 33)	4–8	7.1
		2×10^{-7}(Ref. 62)		
g6SC	1.8	5×10^{-12}	0.8	6.0
g7SC	2.8	(Refs. 33 and 63)	8	5.2

$$K_{\mathrm{US}}^{\mathrm{eff}} = \sum_j^{M_d^{\mathrm{AA}}} \frac{\tau_{n,in}}{\tau_{n,j,in}} K_{\mathrm{US,j}}. \tag{20}$$

Here, $K_{\mathrm{US,j}}$ deals with the j-th defect–ultrasound interaction.

The obtained dependences of $\varepsilon_{\tau n}$ vs W_{US} are shown in Fig. 8. The linearity of these dependences proves the correctness of our assumptions. The obtained $K_{\mathrm{US}}^{\mathrm{eff}}$ values are listed in Table V. The non-monotonic $K_{\mathrm{US}}^{\mathrm{eff}}$ alteration with γ dose is discussed in Sec. III D.

C. Shunt resistance

Figure 9 shows the shunt resistance over the explored temperature range. As seen from the figure, the irradiation results in a decrease in R_{sh}. Also, the R_{sh} temperature dependence changes after γ irradiation. In particular, the shunt resistance decreases with the temperature growth in iSC and nSC, whereas in g6SC and g7SC, the increase in R_{sh} vs T is close to linear in the vicinity of 293 K. It should be noted that the R_{sh} axis is logarithmic in Fig. 9(a) and linear in Fig. 9(b).

The shunt resistance is known[66] to occur in the p–n structure due to several non-mechanical reasons. It can be caused by aluminum particles, macroscopic Si_3N_4 inclusions,

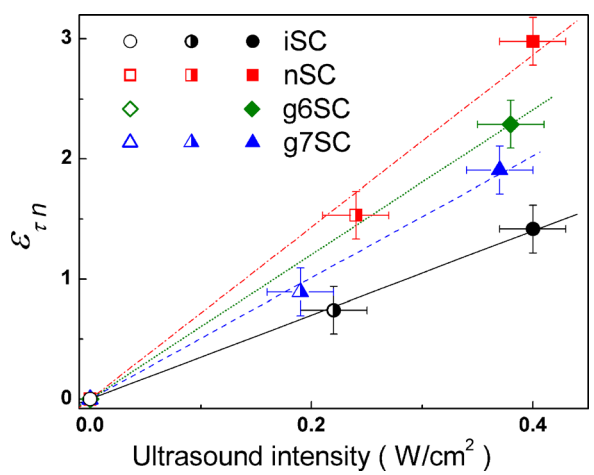

FIG. 8. Dependences of base lifetime relative change on US intensity for non-irradiated (circles), neutron-irradiated (squares), and γ-irradiated (triangles and diamonds) samples. Lines are the fitted curves using Eq. (19).

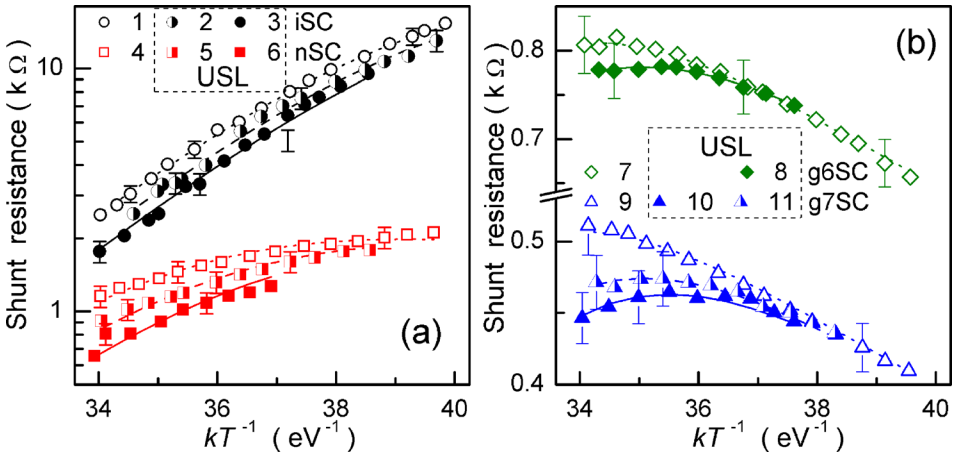

FIG. 9. Temperature dependences of shunt resistance for non-irradiated (curves 1–3, circles), neutron-irradiated (4–6, squares), and γ-irradiated (7–11, diamonds and triangles) samples. The curves 1, 4, 7, and 9 (open marks) are obtained without USL, and curves 2, 3, 5, 6, 8, 10, and 11 correspond to Ui-1, Ui-2, Un-1, Un-2, Ug6-2, Ug7-1, and Ug7-2, respectively. The marks are the experimental results, and the lines are the fitted curves using Eqs. (21)–(23).

or inversion layers at precipitates. In the course of firing, the Al particle can penetrate into the sample creating the p^+-doped region around it, which compensates the emitter and remains in ohmic contact with the base. Inversion layers and Si_3N_4 inclusions occur mainly in multicrystalline silicon cells[66] and cannot cause shunt resistance in the investigated samples. Dislocations, however, which intersect the junction, are generally held responsible as a possible source of ohmic current.[66–68] In our opinion, both aluminum particles and dislocations are present in the investigated structures, so the overall shunt resistance can be expressed as

$$R_{sh}^{-1} = R_{sh,\mathrm{Al}}^{-1} + R_{sh,\mathrm{dis}}^{-1}, \tag{21}$$

where $R_{sh,\mathrm{Al}}$ and $R_{sh,\mathrm{dis}}$ deal with the aluminum particles and dislocations, respectively. The linear temperature dependence of metal particles $R_{sh,\mathrm{Al}}$ is suggested by

$$R_{sh,\mathrm{Al}} = R_{293,\mathrm{Al}}[1 + \alpha(T - 293)], \tag{22}$$

where $R_{293,\mathrm{Al}}$ is the shunt resistance at 293 K and α is the resistance temperature coefficient.

According to the model of dislocation-induced impedance of the photovoltaic detector suggested by Gopal and Gupta,[42,43] $R_{sh,\mathrm{dis}}$ can be given by

$$R_{sh,\mathrm{dis}} = \frac{T}{\sigma_{\mathrm{dis}}}\left[\cosh\left(\frac{E_{\mathrm{dis}} - E_i}{kT}\right) + \cosh\left(\frac{U_s}{kT}\right)\right], \tag{23}$$

with

$$\sigma_{\mathrm{dis}} = \rho_{\mathrm{dis}} A q^2 A_{\mathrm{dis}} \sqrt{K_n K_p}\, N_{\mathrm{dis}}(n_p + p_p)/k, \tag{24}$$

where E_{dis} is the energy level which significantly contributes to the dislocation recombination current, U_s is the potential at the surface of the dislocation core, ρ_{dis} and A_{dis} are the dislocation density and surface area, respectively, K_n and K_p are the probabilities for electrons and holes capture by the dislocation states, and N_{dis} is the density of surface states at each dislocation. Equation (23) is true for the simplified case of $K_p = K_n$.

The resistance temperature coefficient was estimated from data on g7SC. The obtained value 8.3×10^{-3} K^{-1} is not far from the resistance temperature coefficient of bulk Al (4.3×10^{-3} K^{-1}). To fit the experimental data for R_{sh}, we used Eqs. (21)–(23). As the fitting parameters, $R_{293,\mathrm{Al}}$, $(E_{\mathrm{dis}} - E_i)$, U_s, and σ_{dis} were taken. It has been found that the experimental data are in good agreement with the fitting curves (see Fig. 9) for values $(E_{\mathrm{dis}} - E_i) = (0.46 \pm 0.02)$ eV and $U_s = (5 \pm 4) \times 10^{-8}$ eV, which were independent of irradiation and USL. The obtained value of $(E_{\mathrm{dis}} - E_i)$ corresponds to the carrier activation energy 0.10 ± 0.02 eV and is comparable with the activation energy of dislocation levels 0.08 eV, which was earlier reported[69–73] in Cz–Si:B too.[69–71]

The obtained values of $R_{293,\mathrm{Al}}$ and σ_{dis} are given in Table III. $R_{293,\mathrm{Al}}$ does not depend on USL and increases with the irradiation level. In our opinion, $R_{sh,\mathrm{dis}}$ is smaller than $R_{sh,\mathrm{Al}}$ in iSC. The irradiation facilitates the formation of vacancies as well as Al diffusion out of the electrodes. As a consequence, the number of Al particles increases, and $R_{sh,\mathrm{Al}}$ decreases and becomes the key factor contributing to the overall shunt resistance. Al diffuses more effectively in the samples exposed to γ radiation due to a more uniform distribution of irradiation-induced single vacancies.

Dispersion of σ_{dis} correlates with dispersion of τ_n over the sample set. Hence, σ_{dis} dispersion deals with wafer inhomogeneity too. USL causes the σ_{dis} increase, and relative AI changes $\varepsilon_{\sigma\mathrm{dis}} = (\sigma_{\mathrm{dis,US}} - \sigma_{\mathrm{dis},in})/\sigma_{\mathrm{dis},in}$ are shown in Table IV. In our opinion, this is caused by an A_{dis} augmentation. Namely, the dislocation core atom displacement is normal to the current direction. As a result, the carriers are captured by dislocation levels from enlarged volume. Therefore, the effective surface area increases and $R_{sh,\mathrm{dis}}$ decreases due to US action.

D. Defect type speculation

Lifetime killers in boron-doped Czochralski-grown Si are boron–oxygen related (BO) defects,[74,75] iron–boron pairs[64,76,77] (or another Fe-related trap in the n^+p junctions[78,79]), and oxide precipitates.[60,61,64,80–82] The first two defects are sensitive to intensive illumination at room temperature. To determine the major recombination center in the investigated samples, the following experimental procedure was used. The non-irradiated sample was light soaked under illumination using a halogen lamp (2 Suns) at approximately 305 K. The illumination time varied from 1 h to 8 h. After illumination was terminated, the sample was exposed to room temperature in the darkness. Over 5 h period, *I–V*

characteristics were measured with the interval of 10–15 min in order to determine the kinetics of the parameters at room temperature. To estimate the permanent light-induced change, the measurements of *I–V* characteristics were performed in 48 h after illumination. After the total time under illumination ran up to 15 h, the iSC was annealed at 200 °C for 10 min in darkness, after which the measurements were carried out at room temperature. Then, the illumination and measurements were repeated.

Intensive light is known[74,75] to cause permanent transformation of BO defects and considerable decrease in minority–carrier lifetime (as low as 10% of initial value at long term illumination). Annealing at 200 °C for 10 min in the darkness results in both the recovery of state and readiness to light-induced degradation of BO defects. Figure 10 shows the changes of structure parameters in comparison with those prior to illumination. As seen from the figure, illumination does not result in a considerable permanent change of τ_g, τ_n, and n_{id} before as well as after annealing. Therefore, the BO influence on recombination can be neglected in both the SCR and the base.

At the same time, the vast majority of impurity iron exists in iron–boron pairs. Fe_iB_s can be readily dissociated under intense illumination to release interstitial iron, which results in lifetime changes. In the darkness, Fe_iB_s is repaired and Fe_i concentration decreases according to[64,83]

$$N_{Fe}(t) = (N_{Fe,0} - N_{Fe,eq}) \exp\left[-\frac{t}{\tau_{\mathrm{rep}}}\right] + N_{Fe,eq}, \qquad (25)$$

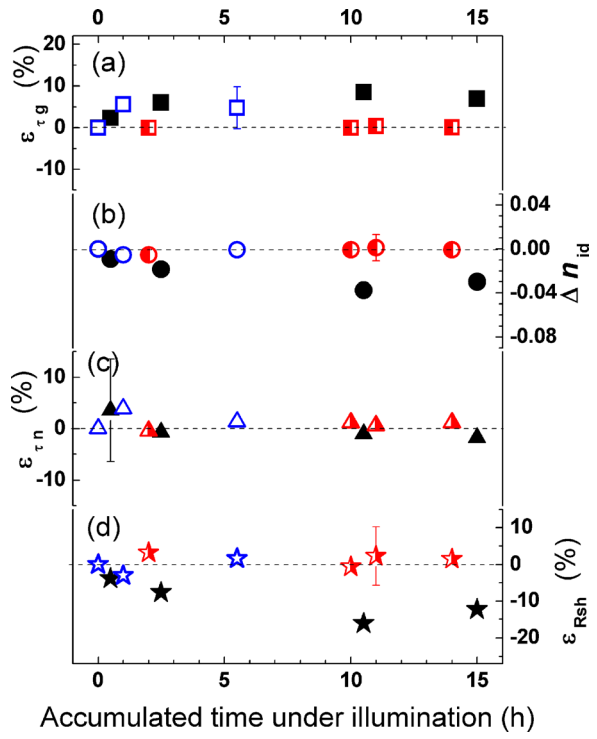

FIG. 10. Permanent changes of SCR lifetime [(a), squares], ideality factor [(b), circles], base lifetime [(c), triangles], and shunt resistance [(d), asterisks] versus accumulated illumination time. Sample iSC, $T = 295$ K. Filled, semi-filled, and open marks correspond to the sample before annealing, after first 10 min 200 °C annealing, and after second 10 min 200 °C annealing, respectively.

where $N_{Fe,0}$ is the concentration immediately after illumination, and $N_{Fe,eq}$ is the equilibrium concentration which remains for a long time after dissociation; the characteristic time of repairing τ_{rep} depends on the doping level

$$\tau_{\mathrm{rep}} = 770 \cdot p_p^{-2/3} \exp\left(\frac{E_{\mathrm{D,Fe}}}{kT}\right), \qquad (26)$$

where $E_{\mathrm{D,Fe}} = 0.68$ eV is the activation energy of Fe_i diffusion.

It was found that n_{id} increased (by about 0.03) and τ_g decreased (by about 10%) immediately after illumination—see Fig. 11(a). These changes vanished gradually. We supposed that τ_g and n_{id} evolutions could be described by expressions similar to Eq. (25). The obtained Eq. (26) was used to calculate characteristic time, and the fitting lines are presented in Fig. 11(a). The fittings with $E_{\mathrm{D,Fe}} = 0.68$ eV are in good agreement with the experimental data. Hence, it is evident that iron–boron pairs take part in SCR recombination. At the same time, electron and hole CCS of Fe_i are 1.7 and 0.04 times[64] as much as those of Fe_iB_s. A small τ_g alteration (by about 10%) caused by light is the evidence of the supporting role of iron–boron pair in SCR recombination. Furthermore, since τ_n does not depend on illumination [see Fig. 11(b)], Fe_iB_s does not influence the base lifetime.

Thus, a conclusion can be made that oxide precipitates are number one agents in SCR and base recombinations. According to Murphy *et al.*[80,81] there exist at least two independent oxide precipitate related defects. These defects have $\sigma_n/\sigma_p = 157$ and $\sigma_p/\sigma_n = 1200$, respectively,[81] which is suitable for CDLR. These facts allow us to conclude that the defect responsible for AI phenomena in iSC is mainly oxide precipitate.

In foreseeing the RD type, it is worth keeping in mind the doping level, oxygen concentration, and irradiation dose. In our case (Czochralski, oxygen-rich, $\sim 7 \times 10^{17}$ cm^{-3}, *p*-Si with boron concentration $\sim 10^{15}$ cm^{-3}, and low dose), it is expected that C_iO_i, vacancy clusters V_n (divacancy V_2, trivacancy V_3,…) and VO_i are produced mainly by neutron irradiation[84–86] while C_iO_i and VO_i are produced by γ-rays.[86–89] The RD concentration $N_{t,\mathrm{RD}}$ linearly depends on the dose, and the known introduction rates for neutron η_n and gamma η_γ irradiation in Cz–Si are shown in Table VI. The expected values of $N_{t,\mathrm{RD}}$ for the investigated samples are listed in Table VI as well.

The other defects that can be created by irradiation in silicon are the I_p center, bistable donor (BD), B_iO_i, and C_iC_s. At the same time, the I_p center and BD are characterized by a small introduction rate. For example, the expected[85,93] concentration of BD is only $(1–2) \times 10^{10}$ cm^{-3} in nSC and g7SC. The lack of B_iO_i in the investigated samples deals with the low boron concentration.[94] The formation of C_iC_s is suppressed in the oxygen-rich crystal[84,87,88] and, what is more, C_iC_s is not an active recombination center.[95]

The influence of RD on base lifetime could be estimated by Eq. (18) taking into account the fact that VO_i is a recombination center which is not active in *p*-Si.[63,96–99] The estimated $\tau_{n,\mathrm{RD}}$ for C_iO_i, V_2, and V_3 are shown in Table VI. As seen from the table, τ_n is effected mainly by C_iO_i in

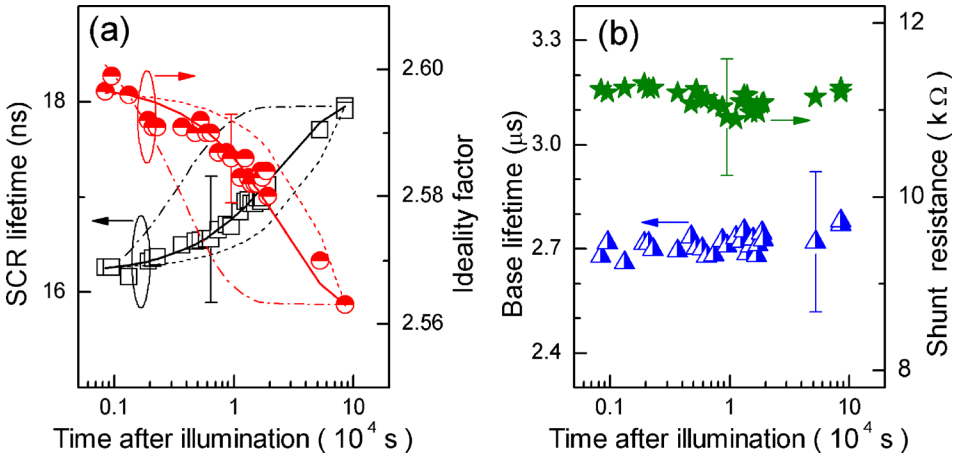

FIG. 11. SCR lifetime [(a), squares, left axis], ideality factor [(a), circles, right axis], base lifetime [(b), triangles, left axis], and shunt resistance [(b), asterisks, right axis] as a function of time since illumination has stopped. Sample iSC, $T = 295$ K. Lines are calculated by using Eqs. (25) and (26) and $E_{D,Fe} = 0.63$ eV (dashed–dotted lines), 0.68 eV (solid lines), and 0.73 eV (dashed lines).

TABLE VI. Cited and calculated defect parameters.

Defect	σ_n (10^{-15} cm^2)	η_n (cm^{-1}) Reference 86	η_γ	$N_{t,RD}$ (10^{11} cm^{-3}) nSC	g6SC	g7SC	$\tau_{n,RD}^{-1}$ (10^4 s^{-1}) nSC	g6SC	g7SC
C_iO_i	0.7 (Ref. 87)	1.38	6×10^5 rad^{-1} cm^{-3} (Ref. 87)	5.5	6	60	0.8–1	0.9–1.1	9–11
	0.9 (Ref. 88)		4×10^{-4} cm^{-1} (Ref. 88)						
V_2	3 (Ref. 87)	1.21	3×10^4 rad^{-1} cm^{-3} (Ref. 87)	4.8	0.3	3	2.2–3.3	0.1–0.2	1–2
	2 (Ref. 90)								
V_3	2.4 (Ref. 91)	0.37	…	1.5	…	…	0.7	…	…
VO_i	2.4 (Ref. 89)	0.52	7×10^5 rad^{-1} cm^{-3} (Ref. 87)	2	6–7	60–70			
	4 (Ref. 92)		4×10^{-4} cm^{-1} (Ref. 88)						

γ-irradiated samples and by vacancy clusters in nSC. It should be noted that nSC, g6SC, and g7SC sums of $\tau_{n,RD}^{-1}$ are in quite good agreement with $(K_\tau \cdot \Psi)$ values.

We shall now consider K_{US}^{eff} for the non-irradiated sample assuming $M_d^{AA} = 1$ and $M_d^{nonAA} = 1$. We shall also assume that US interactions with C_iO_i and V_n are described by K_{US}^{CO} and K_{US}^{V}, respectively. Then, Eq. (20) gives the following expression for K_{US}^{eff} in iSC and irradiated samples:

$$K_{US}^{eff} = K_{US}^{AA}\,\tau_{n,in}/\tau_{n,in}^{AA},$$
$$K_{US}^{eff} = K_{US}^{AA}\tau_{n,in}/\tau_{n,in}^{AA} + K_{US}^{CO}\tau_{n,in}/\tau_{n,RD}^{CO} + K_{US}^{V}\tau_{n,in}/\tau_{n,RD}^{V}.$$

Here, $\tau_{n,in}^{AA}$ is the base lifetime in the sample with the sole non-radiative AA defect and K_{US}^{AA} describes ADI.

For the analysis, the following two limit cases are appropriate. In the first one, non-AA defects are distributed uniformly across the wafer, and AA defects define $(\tau_{n,in}^{-1} - K_\tau \cdot \Psi)$ values in different samples. In the second one, a non-AA defect distribution is not uniform, and $\tau_{n,in}^{AA}$ is identical for iSC, nSC, g6SC, and g7SC. However, in the first case (as well as in the case of $M_d^{nonAA} = 0$), the experimental values of K_{US}^{eff} lead to unreal (negative) values of $K_{US,j}$. In the second case, Eq. (20) and the data from Tables V and VI give the following array equations:

$$\text{iSC}: \; 3.5 = K_{US}^{AA} \cdot (\tau_{n,in}^{AA})^{-1}/2.9,$$
$$\text{nSC}: \; 7.1 = K_{US}^{AA} \cdot (\tau_{n,in}^{AA})^{-1}/4.7 + 0.09\,K_{US}^{V} + 0.02\,K_{US}^{CO},$$
$$\text{g6SC}: \; 6.0 = K_{US}^{AA} \cdot (\tau_{n,in}^{AA})^{-1}/1.8 + 0.01\,K_{US}^{V} + 0.05\,K_{US}^{CO},$$
$$\text{g7SC}: \; 5.2 = K_{US}^{AA} \cdot (\tau_{n,in}^{AA})^{-1}/2.8 + 0.05\,K_{US}^{V} + 0.35\,K_{US}^{CO},$$

where $(\tau_{n,in}^{AA})^{-1}$ in 10^4/s. These equations are valid for $K_{US}^{AA} \cdot (\tau_{n,in}^{AA})^{-1} = (10 \pm 3)$ cm^2/W, $K_{US}^{V} = (42 \pm 15)$ cm^2/W, and $K_{US}^{CO} = 0$. Since $(\tau_{n,in}^{AA})^{-1} < 1.83$, $K_{US}^{AA} > 5$ cm^2/W. Thus, the observed change in base lifetime is caused by AI modification of the same defect (most likely oxide precipitates) in both non-irradiated and γ-irradiated samples. This effect is enhanced by AI alteration of the divacancy in neutron-irradiated samples. In other words, C_iO_i is the non-AA defect, whereas V_2 is the AA defect.

In our opinion, under US action, τ_g and n_{id} in the non-irradiated sample depend on the modification of coupled oxide precipitate related defects. As assumed in Sec. III A, in irradiated samples, the AA radiation defects with $\Delta\Omega_d < 0$ take part in CDLR. The divacancy is a quite suitable explanation for the AI influence on τ_g and n_{id} in nSC, but in γ-irradiated samples, a bistable (or metastable) defect is expected. A few similar defects with $\Delta\Omega_d < 0$ are known in Si, viz, VO_2,[100] V_3,[91] and VO_i.[101] VO_2 is formed after 300 °C annealing of the irradiated crystal, V_3 is not the typical defect for $\gamma-{}^{60}$Co exposed silicon, while VO_i is largo manum produced and can take part in CDLR around n^+–p interface in g6SC and g7SC. The metastable state commonly observed at low temperature is remarkable for the large oxygen–vacancy distance and deeper energy level.[101] The volume change of the entire complex is negative, whereas for the complex component, $\Delta\Omega_d(V) < 0$ and $\Delta\Omega_d(O_i) > 0$. Hence, under the assumption made, VO_i is a favorable pair for AI alteration of the distance between components and therefore can be transformed into the metastable configuration by USL, which causes changes in both T_{id} and $E_{\tau g}$.

IV. CONCLUSION

The influence of ultrasound on *I–V* characteristics of non-irradiated silicon n^+–p structures as well as silicon structures exposed to reactor neutrons or ^{60}Co gamma radiation has been investigated experimentally. The investigation has revealed an acoustically driven reversible decrease in both the minority carrier lifetime and shunt resistance in the structure base. The effect is intensified in the irradiated structures. The analysis has shown that these effects are caused by the acoustically induced increase in the carrier capture coefficient for point or extended defects. It has also been found that ultrasound loading leads to the reversible modification of the SCR carrier lifetime and ideality factor. The changes are opposite in non-irradiated and irradiated structures. The qualitative model of the observed phenomenon, which is based on the increase in the distance between coupled defects or between complex defect components due to ultrasound action, has been suggested. It has been shown that interstitial carbon–interstitial oxygen complexes practically do not take part in acousto–defect interactions, whereas the divacancy in neutron-exposed structures and vacancy–interstitial oxygen pairs in γ-exposed structures can be effectively modified by applying ultrasound. Thus, ultrasound can be an effective tool for controlling silicon structure characteristics.

[1]M. Jivanescu, A. Romanyuk, and A. Stesmans, J. Appl. Phys. **107**, 114307 (2010).
[2]A. Romanyuk, P. Oelhafen, R. Kurps, and V. Melnik, Appl. Phys. Lett. **90**, 013118 (2007).
[3]I. A. Buyanova, S. S. Ostapenko, M. K. Sheinkman, and M. Murrikov, Semicond. Sci. Technol. **9**, 158 (1994).
[4]O. Korotchenkov and H. Grimmliss, Phys. Rev. B **52**, 14598 (1995).
[5]O. Y. Olikh, Semiconductors **43**, 745 (2009).
[6]S. S. Ostapenko and R. E. Bell, J. Appl. Phys. **77**, 5458 (1995).
[7]I. Ostrovskii, O. Korotchenkov, O. Olikh, A. Podolyan, R. Chupryna, and M. T. Cisneros, J. Opt. A: Pure Appl. Opt. **3**, S82 (2001).
[8]D. Kropman, V. Seeman, S. Dolgov, and A. Medvids, Phys. Status Solidi C **13**, 793 (2016).
[9]N. Zaveryukhina, E. Zaveryukhina, S. Vlasov, and B. Zaveryukhin, Tech. Phys. Lett. **34**, 241 (2008).
[10]S. A. Mirsagatov, I. B. Sapaeva, and Z. Nazarov, Inorg. Mater. **51**, 1 (2015).
[11]R. Savkina, A. Smirnov, T. Kryshtab, and A. Kryvko, Mater. Sci. Semicond. Process. **37**, 179 (2015).
[12]M. Virot, R. Pflieger, E. V. Skorb, J. Ravaux, T. Zemb, and H. Mohwald, J. Phys. Chem. C **116**, 15493 (2012).
[13]O. Y. Olikh, K. V. Voytenko, R. M. Burbelo, and J. M. Olikh, J. Semicond. **37**, 122002 (2016).
[14]O. Olikh, Semiconductors **45**, 798 (2011).
[15]A. Davletova and S. Z. Karazhanov, J. Phys. Chem. Solids **70**, 989 (2009).
[16]A. Davletova and S. Z. Karazhanov, J. Phys. D: Appl. Phys. **41**, 165107 (2008).
[17]V. Melnik, Y. Olikh, V. Popov, B. Romanyuk, Y. Goltvyanskii, and A. Evtukh, Mater. Sci. Eng., B **124–125**, 327 (2005).
[18]O. Y. Olikh, K. V. Voytenko, and R. M. Burbelo, J. Appl. Phys. **117**, 044505 (2015).
[19]O. Olikh, Ultrasonics **56**, 545 (2015).
[20]V. N. Pavlovich, Phys. Status Solidi B **180**, 97 (1993).
[21]F. Mirzade, J. Appl. Phys. **110**, 064906 (2011).
[22]R. Peleshchak, O. Kuzyk, and O. Dan'kiv, Ukr. J. Phys. **61**, 741 (2016).
[23]V. D. Krevchik, R. A. Muminov, and A. Y. Yafasov, Phys. Status Solidi A **63**, K159 (1981).
[24]F. Mirzade, J. Appl. Phys. **97**, 084911 (2005).
[25]I. Ostrovskii and O. Korotchenkov, Solid State Commun. **82**, 267 (1992).
[26]O. Olikh and K. Voytenko, Ultrasonics **66**, 1 (2016).
[27]N. Guseynov, Y. Olikh, and S. Askerov, Tech. Phys. Lett. **33**, 18 (2007).
[28]P. Parchinskii, S. Vlasov, and L. Ligai, Semiconductors **40**, 808 (2006).
[29]A. Gorb, O. Korotchenkov, O. Olikh, and A. Podolian, IEEE Trans. Nucl. Sci. **57**, 1632 (2010).
[30]A. O. Podolian, A. B. Nadtochiy, and O. A. Korotchenkov, Tech. Phys. Lett. **38**, 405 (2012).
[31]Y. Olikh, M. Tymochko, and A. Dolgolenko, Tech. Phys. Lett. **32**, 586 (2006).
[32]Y. Olikh and M. Tymochko, Tech. Phys. Lett. **37**, 37 (2011).
[33]H. Jafari and S. Feghhi, Nucl. Instrum. Methods Phys. Res., Sect. A **816**, 62 (2016).
[34]Y. P. Rao, K. Praveen, Y. R. Rani, A. Tripathi, and A. G. Prakash, Nucl. Instrum. Methods Phys. Res., Sect. B **316**, 205 (2013).
[35]M. Moll, H. Feick, E. Fretwurst, G. Lindström, and C. Schütze, Nucl. Instrum. Methods Phys. Res., Sect. A **388**, 335 (1997).
[36]J. Srour, C. Marshall, and P. Marshall, IEEE Trans. Nucl. Sci. **50**, 653 (2003).
[37]A. Junkes, I. Pintilie, E. Fretwurst, and D. Eckstein, Physica B **407**, 3013–3015 (2012).
[38]N. Arutyunov, N. Bennett, N. Wight, R. Krause-Rehberg, V. Emtsev, N. Abrosimov, and V. Kozlovski, Phys. Status Solidi B **253**, 2175 (2016).
[39]C. A. Londos, G. Antonaras, and A. Chroneos, J. Appl. Phys. **114**, 193513 (2013).
[40]A. Schenka and U. Krumbein, J. Appl. Phys. **78**, 3185 (1995).
[41]S. Steingrube, O. Breitenstein, K. Ramspeck, S. Glunz, A. Schenk, and P. P. Altermatt, J. Appl. Phys. **110**, 014515 (2011).
[42]V. Gopal and S. Gupta, IEEE Trans. Electron Devices **50**, 1220 (2003).
[43]V. Gopal and S. Gupta, IEEE Trans. Electron Devices **51**, 1078 (2004).
[44]A. Akkerman, J. Barak, M. Chadwick, J. Levinson, M. Murat, and Y. Lifshitz, Radiat. Phys. Chem. **62**, 301 (2001).
[45]D. Bräunig and F. Wulf, Radiat. Phys. Chem. **43**, 105 (1994).
[46]A. B. Sproul and M. A. Green, J. Appl. Phys. **73**, 1214 (1993).
[47]D. K. Schroder, *Semiconductor Material and Device Characterization*, 3rd ed. (John Wiley & Sons, New Jersey, 2006).
[48]*Solar Cells Materials, Manufacture and Operation*, 2nd ed., edited by A. McEvoy, T. Markvart, and L. Castaner (Academic Press, Oxford, 2013).
[49]K. Wang and M. Ye, Solid-State Electron. **53**, 234 (2009).
[50]D. Schroder, IEEE Trans. Electron Devices **29**, 1336 (1982).
[51]H. Aharoni, T. Ohmi, M. M. Oka, A. Nakada, and Y. Tamai, J. Appl. Phys. **81**, 1270 (1997).
[52]A. S. H. van der Heide, A. Schonecker, J. H. Bultman, and W. C. Sinke, Prog. Photovoltaics: Res. Appl. **13**, 3 (2005).
[53]J. Beier and B. Voss, in *Proceedings of the 23rd IEEE Photovoltaic Specialists Conference, Louisville, KY, USA* (1993), pp. 321–326.
[54]J. M. Shah, Y.-L. Li, T. Gessmann, and E. F. Schubert, J. Appl. Phys. **94**, 2627 (2003).
[55]A. Kaminski, J. J. Marchand, H. E. Omari, A. Laugier, Q. N. Le, and D. Sarti, in *Proceedings of the 25th IEEE Photovoltaic Specialists Conference, Washington, DC, USA* (1996), pp. 573–576.
[56]W. M. Chen, B. Monemar, E. Janzén, and J. L. Lindström, Phys. Rev. Lett. **67**, 1914 (1991).
[57]A. M. Frens, M. T. Bennebroek, A. Zakrzewski, J. Schmidt, W. M. Chen, E. Janzén, J. L. Lindström, and B. Monemar, Phys. Rev. Lett. **72**, 2939 (1994).
[58]O. Breitenstein, J. Bauer, P. P. Altermatt, and K. Ramspeck, Solid State Phenom. **156–158**, 1 (2010).
[59]T. Wosinski, A. Makosa, and Z. Witczak, Semicond. Sci. Technol. **9**, 2047 (1994).
[60]L. Chen, X. Yu, P. Chen, P. Wang, X. Gu, J. Lu, and D. Yang, Sol. Energy Mater. Sol. Cells **95**, 3148 (2011).
[61]J. Schön, A. Youssef, S. Park, L. E. Mundt, T. Niewelt, S. Mack, K. Nakajima, K. Morishita, R. Murai, M. A. Jensen, T. Buonassisi, and M. C. Schubert, J. Appl. Phys. **120**, 105703 (2016).
[62]E. Gaubas, A. Uleckas, and J. Vaitkus, Nucl. Instrum. Methods Phys. Res., Sect. A **607**, 92 (2009).
[63]I. I. Kolkovskii, P. F. Lugakov, and V. V. Shusha, Phys. Status Solidi A **83**, 299 (1984).
[64]J. D. Murphy, K. Bothe, M. Olmo, V. V. Voronkov, and R. J. Falster, J. Appl. Phys. **110**, 053713 (2011).
[65]D. G. Thomas, J. Hopfield, and W. M. Augistyniak, Phys. Rev. **140**, A202 (1965).
[66]O. Breitenstein, J. P. Rakotoniaina, M. H. Al Rifai, and M. Werner, Prog. Photovoltaics: Res. Appl. **12**, 529 (2004).
[67]V. Gopal, J. Appl. Phys. **116**, 084502 (2014).
[68]I. Baker and C. Maxey, J. Electron. Mater. **30**, 682 (2001).

[69]A. Castaldini, D. Cavalcoli, A. Cavallini, and S. Pizzini, Phys. Rev. Lett. **95**, 076401 (2005).
[70]I. Isakova, A. Bondarenko, O. Vyvenko, V. Vdovin, E. Ubyivovk, and O. Kononchuk, J. Phys.: Conf. Ser. **281**, 012010 (2011).
[71]X. Yu, O. Vyvenko, M. Kittler, W. Seifert, T. Mtchedlidze, T. Arguirov, and M. Reiche, Semiconductors **41**, 458 (2007).
[72]V. Kveder, M. Kittler, and W. Schröter, Phys. Rev. B **63**, 115208 (2001).
[73]M. Trushin, O. Vyvenko, T. Mchedlidze, O. Kononchuk, and M. Kittler, Solid State Phenom. **156–158**, 283 (2010).
[74]J. Lindroos and H. Savin, Sol. Energy Mater. Sol. Cells **147**, 115 (2016).
[75]T. Niewelt, J. Schöon, W. Warta, S. W. Glunz, and M. C. Schubert, IEEE J. Photovoltaics **7**, 383 (2017).
[76]V. Vahanissi, A. Haarahiltunen, H. Talvitie, M. Yli-Koski, and H. Savin, Prog. Photovoltaics: Res. Appl. **21**, 1127 (2012).
[77]J. Schmidt, Prog. Photovoltaics: Res. Appl. **13**, 325 (2005).
[78]T. Mchedlidze and J. Weber, Phys. Status Solidi B **251**, 1608 (2014).
[79]T. Mchedlidze, L. Scheffler, J. Weber, M. Herms, J. Neusel, V. Osinniy, C. Moller, and K. Lauer, Appl. Phys. Lett. **103**, 013901 (2013).
[80]J. Murphy, J. McGuire, K. Bothe, V. Voronkov, and R. Falster, Sol. Energy Mater. Sol. Cells **120**, 402 (2014).
[81]J. D. Murphy, K. Bothe, R. Krain, V. V. Voronkov, and R. J. Falster, J. Appl. Phys. **111**, 113709 (2012).
[82]M. Porrini and P. Tessariol, Mater. Sci. Eng. B **73**, 244 (2000).
[83]W. Wijaranakula, J. Etectrochem. Soc. **140**, 275 (1993).
[84]G. Lindström, M. Ahmed, S. Albergo, P. Allport, D. Anderson, L. Andricek, M. Angarano, V. Augelli, N. Bacchetta, P. Bartalini, R. Bates, U. Biggeri, G. Bilei, D. Bisello, D. Boemi, E. Borchi, T. Botila, T. Brodbeck, M. Bruzzi, T. Budzynski, P. Burger, F. Campabadal, G. Casse, E. Catacchini, A. Chilingarov, P. Ciampolini, V. Cindro, M. Costa, D. Creanza, P. Clauws, C. Da Via, G. Davies, W. De Boer, R. DellOrso, M. D. Palma, B. Dezillie, V. Eremin, O. Evrard, G. Fallica, G. Fanouraki, H. Feick, E. Focardi, L. Fonseca, E. Fretwurst, J. Fuster, K. Gabathuler, M. Glaser, P. Grabiec, E. Grigorievt, G. Hall, M. Hanlond, F. Hauler, S. Heising, A. Holmes-Siedle, R. Horisberger, G. Hughes, M. Huhtinen, I. Ilyashenko, A. Ivanov, B. Jones, L. Jungermann, A. Kaminsky, Z. Kohout, G. Kramberger, M. Kuhnke, S. Kwan, F. Lemeilleur, C. Leroy, M. Letheren, Z. Li, T. Ligonzo, V. Linhart, P. Litovchenko, D. Loukas, M. Lozano, Z. Luczynski, G. Lutz, G. MacEvoy, S. Manolopoulos, A. Markou, C. Martinez, A. Messineo, M. Mikuž, M. Moll, E. Nossarzewska, G. Ottaviani, V. Oshea, G. Parrini, D. Passeri, D. Petre, A. Pickford, I. Pintilie, L. Pintilie, S. Pospisil, R. Potenza, C. Raine, J. Rafi, P. Ratoff, H. Richter, P. Riedler, S. Roe, P. Roy, A. Ruzin, A. Ryazanov, A. Santocchia, L. Schiavulli, P. Sicho, I. Siotis, T. Sloan, W. Slysz, K. Smith, M. Solanky, B. Sopko, S. K. B. Sundby Avset, S. B. C. Tivarus, G. Tonelli, A. Tricomi, S. Tzamarias, G. Valvo, A. Vasilescu, A. Vayaki, E. Verbitskaya, P. Verdini, V. Vrba, S. Watts, E. Weber, M. Wegrzecki, I. Wegrzecka, P. Weilhammer, R. Wheadon, C. Wilburn, I. Wilhelm, R. Wunstorf, J. Wüstenfeld, J. Wyss, K. Zankel, P. Zabierowski, and D. Žontar, Nucl. Instrum. Methods Phys. Res., Sect. A **466**, 308 (2001).
[85]I. Pintilie, G. Lindstroem, A. Junkes, and E. Fretwurst, Nucl. Instrum. Methods Phys. Res., Sect. A **611**, 52 (2009).
[86]M. Moll, "Radiation damage in silicon particle detectors: Microscopic defects and macroscopic properties," Ph.D. thesis (Universität Hamburg, 1999).
[87]J. Stahl, E. Fretwurst, G. Lindström, and I. Pintilie, Nucl. Instrum. Methods Phys. Res., Sect. A **512**, 111 (2003).
[88]I. I. Kolkovskii and V. Lukyanitsa, Semiconductors **31**, 340 (1997).
[89]R. Siemieniec, W. Sudkamp, and J. Lutz, in *Proceedings of the Fourth IEEE International Caracas Conference on Devices, Circuits and Systems* (Oranjestad, Aruba, Netherlands, 2002), pp. D029–1–D029–6.
[90]S. D. Brotherton and P. Bradley, J. Appl. Phys. **53**, 5720 (1982).
[91]V. P. Markevich, A. R. Peaker, S. B. Lastovskii, L. I. Murin, J. Coutinho, V. J. B. Torres, P. R. Briddon, L. Dobaczewski, E. V. Monakhov, and B. G. Svensson, Phys. Rev. B **80**, 235207 (2009).
[92]H. Bleichner, P. Jonsson, N. Keskitalo, and E. Nordlander, J. Appl. Phys. **79**, 9142 (1996).
[93]E. Fretwurst, F. Hönniger, G. Kramberger, G. Lindström, I. Pintilie, and R. Röder, Nucl. Instrum. Methods Phys. Res., Sect. A **583**, 58 (2007).
[94]L. C. Kimerling, M. Asom, J. Benton, P. Drevinsky, and C. Caefer, Mater. Sci. Forum **38–41**, 141 (1989).
[95]L. W. Song, X. D. Zhan, B. W. Benson, and G. D. Watkins, Phys. Rev. B **42**, 5765 (1990).
[96]J. L. Benton, S. Libertino, P. Kringhøj, D. J. Eaglesham, J. M. Poate, and S. Coffa, J. Appl. Phys. **82**, 120 (1997).
[97]S. Coffa, V. Privitera, F. Priolo, S. Libertino, and G. Mannino, J. Appl. Phys. **81**, 1639 (1997).
[98]N. Ganagona, B. Raeissi, L. Vines, E. V. Monakhov, and B. G. Svensson, Phys. Status Solidi C **9**, 2009 (2012).
[99]L. Vines, E. V. Monakhov, A. Y. Kuznetsov, R. Kozłowski, P. Kaminski, and B. G. Svensson, Phys. Rev. B **78**, 085205 (2008).
[100]L. I. Murin, V. P. Markevich, I. F. Medvedeva, and L. Dobaczewski, Semiconductors **40**, 1282 (2006).
[101]B. N. Mukashev, K. A. Abdullin, and Y. V. Gorelkinskii, Phys.–Usp. **43**, 139 (2000).